PAPER • OPEN ACCESS

4D dosimetric-blood flow model: impact of prolonged fraction delivery times of IMRT on the dose to the circulating lymphocytes

View the article online for updates and enhancements.

Physics in Medicine & Biology

IPEM
Institute of Physics and
Engineering in Medicine

CrossMark

PAPER

4D dosimetric-blood flow model: impact of prolonged fraction delivery times of IMRT on the dose to the circulating lymphocytes

Abdelkhalek Hammi ⬡

TU Dortmund University, Dortmund, Germany

E-mail: abdelkhalek.hammi@tu-dortmund.de

Abstract

To investigate the impact of prolonged fraction delivery of modern intensity-modulated radiotherapy (IMRT) on the accumulated dose to the circulating blood during the course of fractionated radiation therapy. We have developed a 4D dosimetric blood flow model (d-BFM) capable of continuously simulating the blood flow through the entire body of the cancer patient and scoring the accumulated dose to blood particles (BPs). We developed a semi-automatic approach that enables us to map the tortuous blood vessels of the surficial brain of individual patients directly from standard magnetic resonance imaging data of the patient. For the rest of the body, we developed a fully-fledged dynamic blood flow transfer model according to the International Commission on Radiological Protection human reference. We proposed a methodology enabling us to design a personalized d-BFM, such it can be tailored for individual patients by adopting intra- and inter-subject variations. The entire circulatory model tracks over 43 million BPs and has a time resolution of $\Delta t = 10^{-3}$ s. A dynamic dose delivery model was implemented to emulate the spatial and temporal time-varying pattern of the dose rate during the step-and-shoot mode of IMRT. We evaluated how different configurations of the dose rate delivery, and a time prolongation of fraction delivery may impact the dose received by the circulating blood (CB). Our calculations indicate that prolonging the fraction treatment time from 7 to 18 min will augment the blood volume receiving any dose $V_{D>0\mathrm{Gy}}$ from 36.1% to 81.5% during one single fraction. The results indicate that increasing the segment number has only a negligible effect on the irradiated blood volume, when the fraction time is kept identical. We developed a novel concept of customized 4D d-BFM that can be tailored to the hemodynamics of individual patients to quantify dose to the CB during fractionated radiotherapy. The prolonged fraction delivery and the variability of the instantaneous dose rate have a significant impact on the accumulated dose distribution during IMRT treatments. This impact should be considered during IMRT treatments design to reduce RT-induced immunosuppressive effects.

1. Introduction

1.1. Radiation to circulating blood and lymphopenia is crucial

Cancer radiotherapy (RT) exerts a double and opposite effect on the antitumor immune response (llavena *et al* 2008). It has the potential to affect the tumor microenvironment, increasing infiltration of natural killer cells, T-cells, and other leukocytes that could inhibit tumor growth (Ni *et al* 2012, Klug *et al* 2013). On the other hand, RT could modulate immunosuppressive properties, including lymphopenia (i.e. lower than the baseline total lymphocytes count) and contribute to tumor growth (llavena *et al* 2008, Aymeric *et al* 2010). Recent clinical evidence across multiple cancer sites and treatment modalities showed that lymphopenia is associated with poor outcome in cancer patients (Wu *et al* 2014, Diehl *et al* 2017, Ho *et al* 2018, Cho *et al* 2019, Kleinberg *et al* 2019, Karantanos *et al* 2019). Clinical studies have reported that RT-induced lymphopenia is associated with the gross tumor volume in lung patients and that its severity can be reduced by reducing dose exposure to the heart, peripheral blood, and the lymphoid organs (Contreras *et al* 2018, Joseph *et al* 2019). Based on this evidence, we

hypothesize that optimizing the RT delivery protocol has the potential to lower RT-induced immunosuppressive effects by mitigating or even preventing RT-related lymphopenia.

Nowadays, there is no quantitative evidence to establish a direct connection between the integral dose and the dose-rate delivery to critical normal structures and RT-induced lymphopenia. However, recently, a few studies have been conducted to improve our understanding of how external RT delivery parameters could affect the depletion of circulating lymphocytes in patients (Yovino *et al* 2013, Basler *et al* 2018, Hammi *et al* 2020, Shin *et al* 2021, Xing *et al* 2022). Yovino *et al* (2013) developed a mathematical formalism to compute radiation dose to circulating lymphocytes. The model was composed of a dual compartment: the brain, which contains the blood passing through the radiation field without re-circulation, and the rest of the body. Based on patients with high-grade glioma, the study investigated how the size of the target, the administered fractionation and the dose rate can affect the severity of lympho-toxicity. Hammi *et al* (2020) implemented an explicit 4D Monte Carlo tool to compute the instantaneous and accumulated dose to peripheral blood. The approach encompasses two independent models: a beam delivery model that reproduces the dynamic dose rate inside the patient, and a blood flow model (BFM) that simulates the spatiotemporal distribution of blood particles (BPs) through the field. The authors proposed to extract the cerebral arterial and venous vasculatures from Magnetic resonance imaging (MRI) data to simulate blood flow pathways. The entire body's blood circulation was modeled according to a human body model (Leggett and Williams 1995) and was based on hemodynamics references (organ blood volume and flow rate) of the ICRP report 89 (ICRP89 2002). The blood transport outside the brain was simulated by assuming a compartment model and using a discrete-time Markov Chain (DTMC). Shin *et al* (2021) proposed a compartment model based on ICRP report 89 to model circulating blood (CB) and used dose volume histogram (DVH) information based on the treatment plan instead of modeling the beam delivery explicitly. The approach samples the DVH of the irradiated organs over the fraction delivery time to simulate a time-dependent organ DVH. The BPs spatial distribution was calculated based on a DTMC process and by assuming a Weibull distribution to simulate a variable transition probability.

1.2. Limitations of dose calculation to circulating blood approaches

The few currently published methods are based on several simplifying assumptions and many potential factors are not explicitly considered and remain confounding factors:
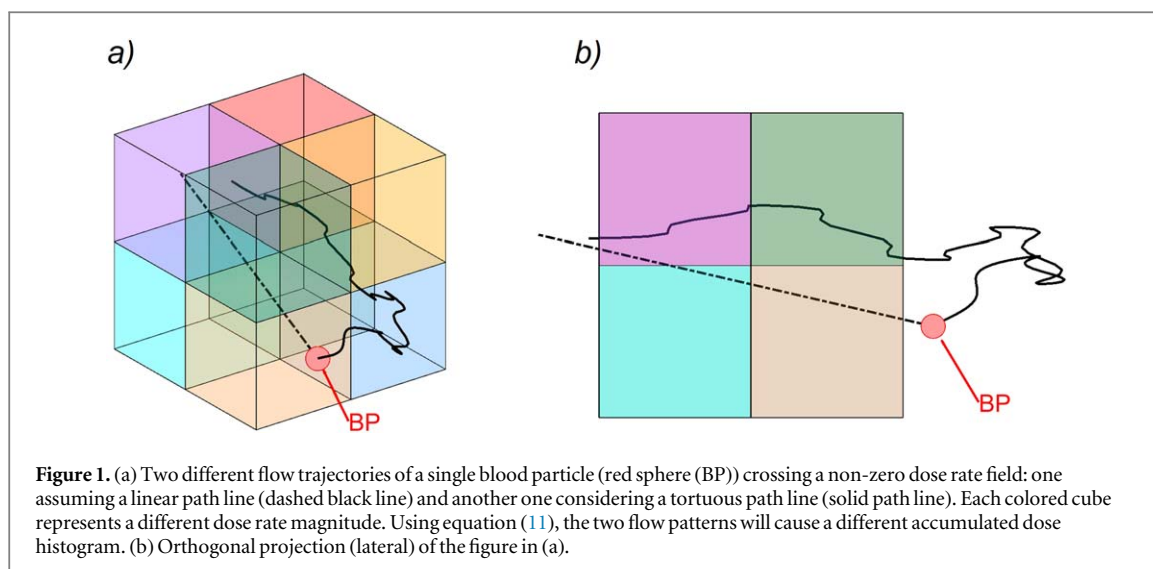
1.2.1. Customized hemodynamics

Hemodynamic values from ICRP report 89 (for more information, see Hammi *et al* (2020) and Shin *et al* (2021) are the most established consensus references known to approximate human blood circulation. The values were derived from a multi-institutional study and were collected over a large population. Yet, uncertainties arising from intra- and inter-subject variations and errors in measurement techniques were not considered, which are relatively high with 60% (Hoskins 1996, Jiang *et al* 2011). In addition, the references represent just the baseline values for a healthy, reclining, 35 years old male (Leggett and Williams 1995). Thus, the references may neither be accurate nor representative of differentiated patient circulatory systems.

1.2.2. Realistic vascular morphology

Segmenting the entire cerebral vessel network from standard imaging techniques is difficult, especially in the case of the human brain. Hammi *et al* (2020) proposed a hybrid cerebral vessel model by explicitly segmenting the large vessels from MRI images (about 5% of the total vasculature) and extending it with a generic vascular model to approximate the blood distribution inside the brain volume. Although such a generic configuration can be convenient for systematic evaluations and for a general understanding, for the case of a high spatiotemporal analysis, such as quantifying blood flow velocity vector fields crossing short-pulsed beam delivery, a more realistic and patient-specific vasculature architecture is of crucial importance. Indeed, complex bifurcations, the tortuosity, and the curvature degree of the vessels will directly affect the geometrical blood flow distribution inside the brain (Duvernoy 1999), and therefore the accumulated dose to the CB. Results from unpublished data showed that less realistic blood path lines underestimate the positional distribution of the blood volume inside the dose rate grid and therefore underestimate the blood volume receiving any dose ($V_{D>0\text{Gy}}$) by roughly 29% and results in a mean dose difference of up to 12% for a clinical plan with four fields (figure 1).

1.2.3. Simplified fraction delivery model

The previous published studies were based on a simplified fraction delivery: the delivery models sampled the total planned (or a single field) dose distribution over the corresponding delivery time to compute a constant dose rate. Such simplifications do not incorporate the instantaneous dose rate variation within the patient as a function of time, which is crucial for an accurate quantification of the dose to CB via modern delivery

Figure 1. (a) Two different flow trajectories of a single blood particle (red sphere (BP)) crossing a non-zero dose rate field: one assuming a linear path line (dashed black line) and another one considering a tortuous path line (solid path line). Each colored cube represents a different dose rate magnitude. Using equation (11), the two flow patterns will cause a different accumulated dose histogram. (b) Orthogonal projection (lateral) of the figure in (a).

techniques. This is because the dose rate of modern techniques such IMRT (e.g. step-and-shoot and sliding window), volumetric modulated arc therapy (VMAT), and proton pencil-beam scanning varies continuously.

1.3. Motivation of the work

To improve our understanding of how dose received by peripheral blood during external RT potentially affects the depletion of lymphocytes in brain patients, there is an increased need for a less generic and more subject-specific brain BFM that reflects a more realistic configuration of the cerebral vasculatures and personalized hemodynamics. In addition, a realistic dynamic delivery model capable of simulating variations of the dose-rate inside the patient is necessary to assess the effect of variable delivery times of modern RT techniques. In this work, we introduce a novel concept of personalized 4D dosimetric-BFM (d-BFM). The presented work has three complimentary primary motivations:
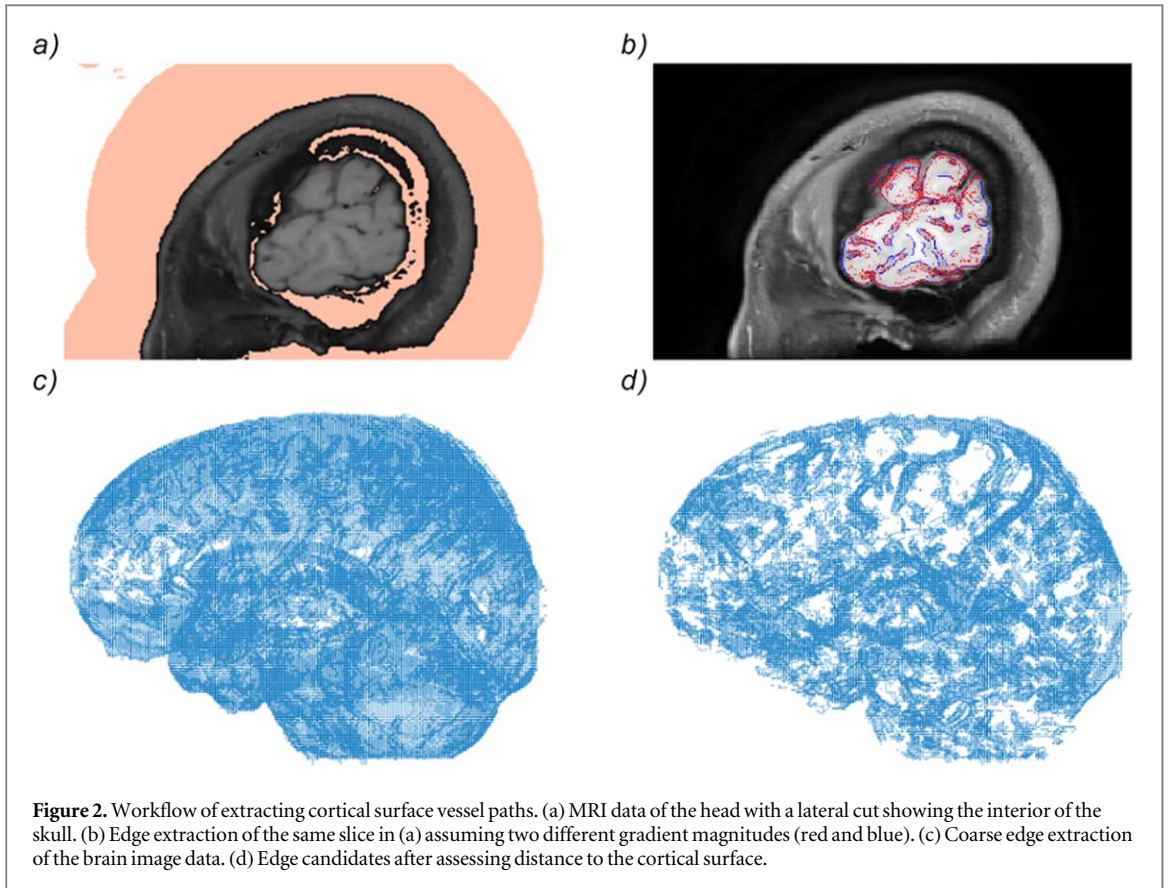
1.3.1. Tortuous blood vessels

Studies have reported that over 70% of the blood flow rate coming from the internal carotid arteries to the brain flows through the middle cerebral artery (Zarrinkoob *et al* 2015). These arteries occupy the space between the cortical folding (i.e. gyri and sulci) to supply the lateral surface of the cerebral hemisphere while also adapting to the overhanging surface morphology of the brain (Duvernoy 1999). In this work, we developed a framework capable of extracting the tortuous cerebral blood vessel network directly from standard MRI images of the patient. The extraction approach operates semi-automatically to guarantee reproducibility and to reduce the delineation workload. The curvature of the blood vessels is based on the indentations and folding of the cerebral cortex.

1.3.2. Customized blood flow mode

Hammi *et al* (2020) considered the compartments as homogeneous entities in their BFM. The inflowing blood was assumed well-mixed, and it was instantaneously distributed within the compartment. This simplification did not account for residence time of the BPs inside the compartment. Shin *et al* (2021) proposed a time-varying transition probability that increases the probability of a BP to outflow with increasing dwell time inside the same compartment. Furthermore, DTMC-based methods are generally limited by the uniform time step discretization and by the synchronous discrete-time state changes that are less characteristic of a continuous-time dynamic system.

   To improve the approximation of the underlying perfusion processes of the explicit Monte Carlo-based BFM, we propose a novel compartmental blood flow design that involves the three functional structures of the blood vessel (i.e. artery, capillary, and vein) in each individual compartment to account for the transition time of BPs. In addition, we propose a technique that enables the integration of any additional information about the physiological blood flow of the patient into the development of a personalized and less standardized BFM. Such physiological blood flow information could be obtained using advanced functional imaging methods, including 4D flow MRI (as demonstrated in Zhuang *et al* (2021)) or 4D ultrasound (as shown in Correia *et al* (2016)), among other available options.

Figure 2. Workflow of extracting cortical surface vessel paths. (a) MRI data of the head with a lateral cut showing the interior of the skull. (b) Edge extraction of the same slice in (a) assuming two different gradient magnitudes (red and blue). (c) Coarse edge extraction of the brain image data. (d) Edge candidates after assessing distance to the cortical surface.

1.3.3. Realistic dynamic dose delivery

IMRT treatment plans typically comprise 5–9 directional beams, and each of the beams comprises 10–50 segments, resulting in at least 50 segments for the entire plan. Segment shaping requires a few seconds to steer the motor-driven leaves to change the shape of the previous aperture to the current one. The speed of the leaves is restricted to up 2.7 s cm^{-1} by the vendor. The resulting delay produces a nonuniform spatio-temporal pattern of the dose delivery inside the patient and imposes a prolongation of the treatment time of up to 10 times compared to conventional 3D-conformal RT (Wang *et al* 2003). We investigated how instantaneous $\dot{D}(t)$ and constant $\overline{\dot{D}}$ dose rates and the overall treatment time of step-and-shoot IMRT impact the accumulated dose to CB.

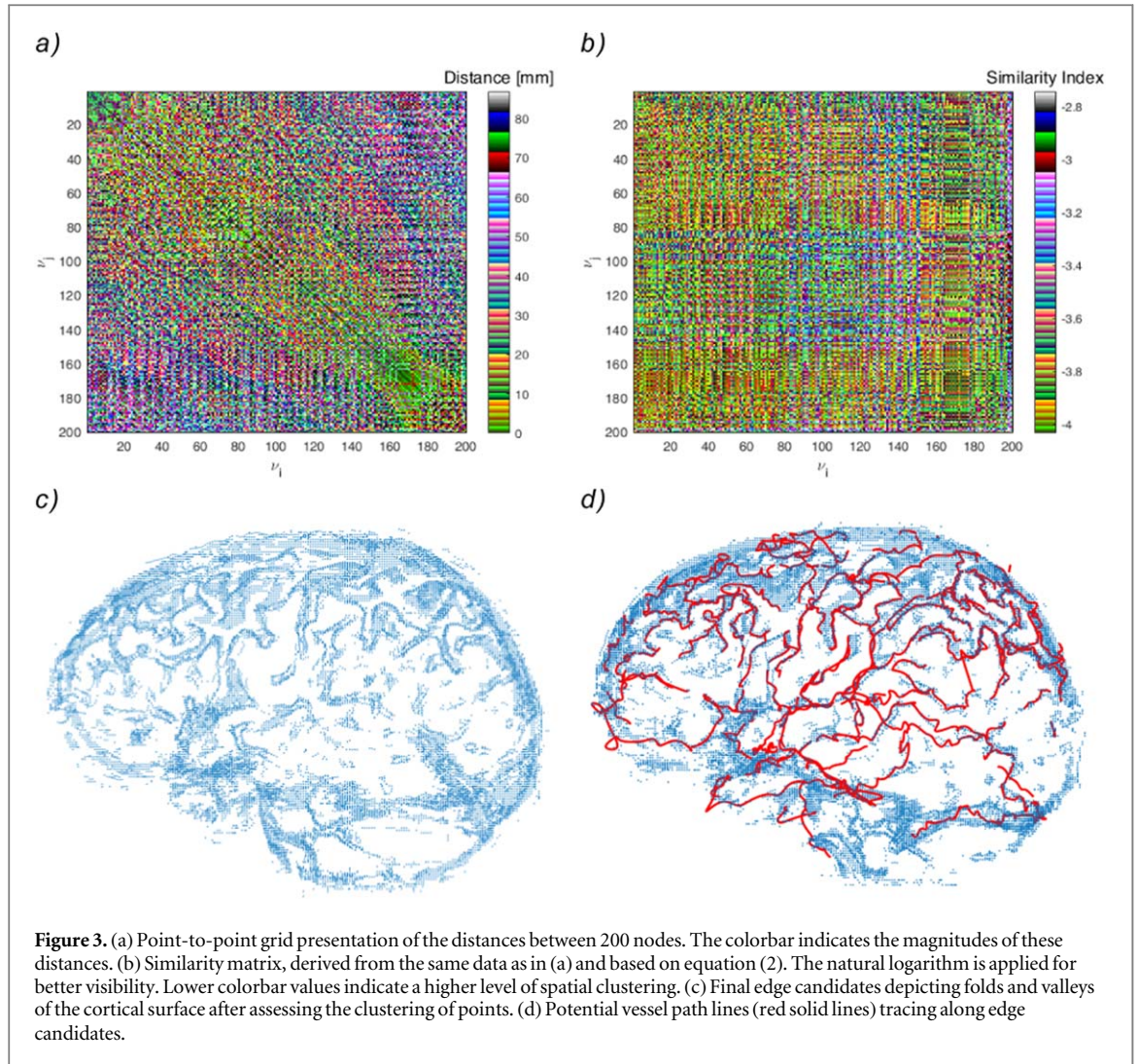## 2. Methods and materials

2.1. Vasculature

The automatic surficial blood vessel approach proposed in this work comprises three successive steps: (1) extraction of the edges of the folds and grooves in the cerebral cortex based on their topographic properties, (2) calculation of the affinity between the edges to assess their clustering degree, and (3) connecting the final candidate edges to trace curves along the folds as path lines for cerebral blood flow.

2.1.1. Topographic cortical surface edge extraction

The image data used in this study comprises openly accessible black-blood T1-weighted MRI brain images with isotropic voxels which are 0.85 mm in size (Absinta *et al* 2017). The image data was subject to three successive steps of edge detection operations: image smoothing, image differentiation, and edge labeling. An anisotropic diffusion smoothing filter was applied to gradually filter out noise of the image while preserving the edge features (Perona and Malik 1990). A standard gradient threshold method was performed to achieve coarse edges (see figure 2(b&c)). Finally, we computed the projected distance $\hat{d}_i$ of each candidate's edge $v^i = \{v^1, \dots, \dots v^n\}$ on the cortical surface:

$$\hat{d}_i = \|(g''_i - g'_i) \cdot v^i)\| / \|(g''_i - g'_i)\| \tag{1}$$

where g'_i is the closest point to the vertex v^i found on the closest cortical geodesic G_i and g''_i is the normal projection of g'_i onto the line segment $\overline{v^i g'_i}$. Sulcal depths are reported to reach a depth of at least 10 mm

Figure 3. (a) Point-to-point grid presentation of the distances between 200 nodes. The colorbar indicates the magnitudes of these distances. (b) Similarity matrix, derived from the same data as in (a) and based on equation (2). The natural logarithm is applied for better visibility. Lower colorbar values indicate a higher level of spatial clustering. (c) Final edge candidates depicting folds and valleys of the cortical surface after assessing the clustering of points. (d) Potential vessel path lines (red solid lines) tracing along edge candidates.

(Kao *et al* 2007). In our work, a threshold depth was empirically set to 2 mm and was found to appropriately capture ridges (see figure 2d).

2.1.2. Probabilistic clustering and path line tracing

The density of the edges is highest along folds and decreases along valleys, where the image intensity barely changes (figure 2d). To improve capturing true folds despite the cluttered background, we assume that less clustered edges are noisy. We computed the point-to-point similarity matrix to assess the clustering level of each candidate vertex with their neighbors (Ng *et al* 2001). The Gaussian affinity matrix $M_A \in \mathcal{R}^{nxn}$ is defined as:
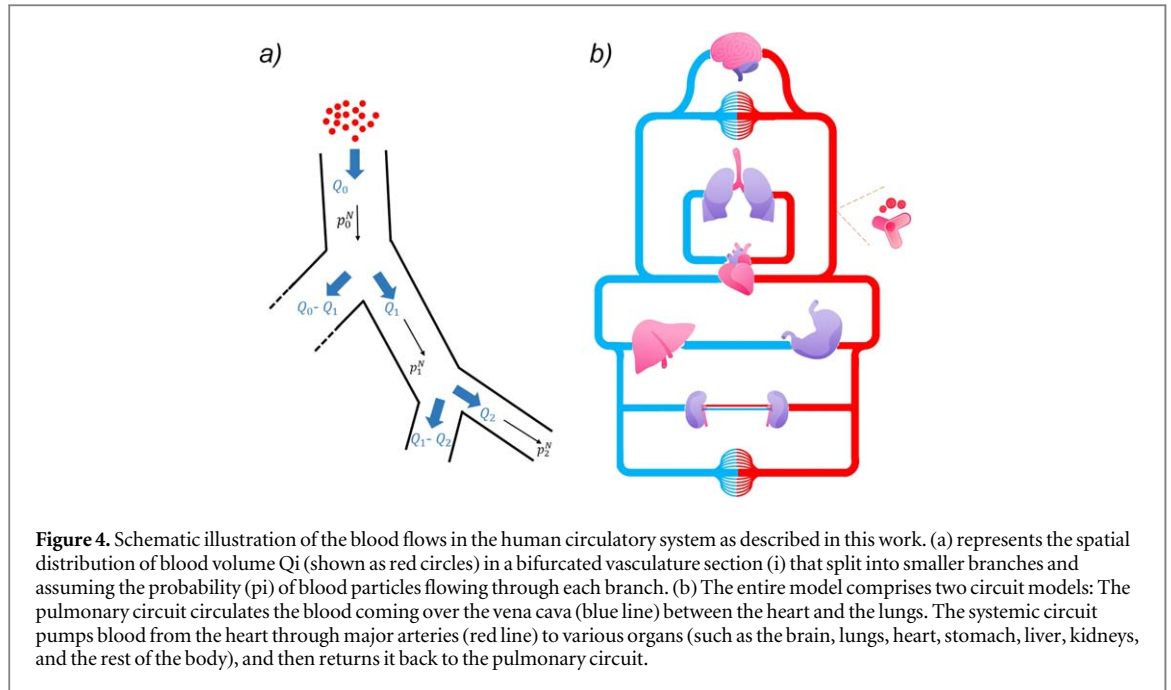
$$M_A(v_i, v_j) = \frac{1}{\sqrt{2\pi}\sigma_i \sigma_j} \exp\left(\frac{(x_i - x_j)^2}{\sigma_i \sigma_j}\right), \ i \neq j, \tag{2}$$

where v_j is the jth neighbor surrounding v_i with the coordinates x_i. σ_i describes the distance distribution between v_i and their neighbors:

$$\sigma(v_i) = \sqrt{\frac{1}{n_k}\sum_{k=1}^{n_k}(x_i - x_{k,i})^2}, \tag{3}$$

where $x_{k,i}$ is the coordinate of the closest kth neighbor to v_i. In our approach, this number was empirically set to $n_k = 15$, which was found to give good clustering results. According to the definition, noise and scattered points will have higher values than denser distributed vertices and can thus be filtered out Ng *et al* (2001), (see figure 3(a&b)).

Tracing cortical blood flow trajectories from final candidate points comes down to finding the shortest path that interconnects the ultimate points, starting from a source (s_i) and target (t_i) pair nodes. To guarantee more realistic curvatures, we manually specified control nodes (c_i) through which trajectories must cross. Those must-travel junctions were directly sampled from MRI images. Dijkstra's algorithm was then applied to

Figure 4. Schematic illustration of the blood flows in the human circulatory system as described in this work. (a) represents the spatial distribution of blood volume Qi (shown as red circles) in a bifurcated vasculature section (i) that split into smaller branches and assuming the probability (pi) of blood particles flowing through each branch. (b) The entire model comprises two circuit models: The pulmonary circuit circulates the blood coming over the vena cava (blue line) between the heart and the lungs. The systemic circuit pumps blood from the heart through major arteries (red line) to various organs (such as the brain, lungs, heart, stomach, liver, kidneys, and the rest of the body), and then returns it back to the pulmonary circuit.

compute the shortest distance path dist(s_i, c_i, t_i) between each of these sequential seed pairs (Dijkstra 1959). To search for multiple trajectories with different topologies with no additional selection of start-target pair nodes, the ideal path line is computed $P^{(s_i, t_i)}$. The corresponding nodes were then progressively pruned and substituted with a new node set randomly picked from the neighbor points within an arbitrary distance r_i, and a different trajectory is calculated. This is equivalent to introducing a probability distortion to deviate ideal trajectories. The pseudo-code below at the end of this sub-section describes the algorithm introduced here. We used the approach to trace venous vessels that flow in vicinity of the arterial vessel.

2.2. Blood flow

2.2.1. Human body model

We developed a human-like cardiovascular compartment model to simulate the spatiotemporal distribution of the BPs throughout the entire body (figure 4). The compartment system has a modular design and was structured according to ICRP report 89. Large organs that extend continuously throughout the entire body (e.g. lymph nodes, skin, muscle…) were split into two sub-compartments to distinguish between the upper and the lower limbs' blood supply (i.e. lower body muscles and upper body muscles). The entire compartment system incorporates 32 different organs (Hammi *et al* 2020). Inside the brain where the change in dose $\dot{D}(t)$ can be greater than zero, the blood flow is explicitly simulated. BPs are propagated along the path lines at a local speed $\vec{V}(x)$. In the rest of the body, the blood flow is approximated by DTMC (Hammi *et al* 2020, Shin *et al* 2021) (figure 5(a)). The state transition probability from compartments $i \rightarrow j$ is:
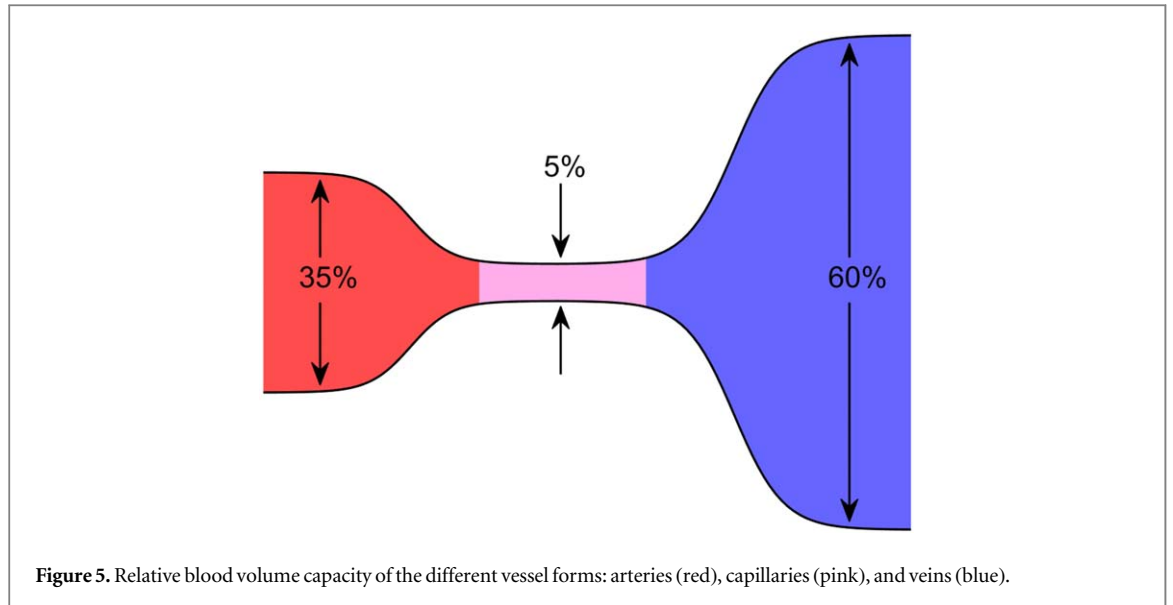
$$p_{i \rightarrow j} = \frac{\text{CO} * b_F^{ij}}{\text{HR} * b_V^i * V_B},$$

(4)

where CO is the cardiac output [l min^{-1}], b_F^{ij} is the blood flow rate from organ i to j in % of cardiac output, HR is the heart rate [beats per min], and b_V^i is the regional blood content in % of the total blood volume V_B [l]. The state time evolution is discrete and advances in time by the heart rate:

$$\Delta T_{\text{HB}} = \frac{60}{\text{HR}}[s].$$

2.2.2. Blood attenuation time in compartment

We translated individual compartments into three nested sub-compartments to account for transit time. Each of the sub-compartments presents one of the three functional structures of the blood vessel (i.e. artery, capillary, and vein). The relative blood reservoirs are: $\mu_i^a = 35\%$, $\mu_i^c = 5\%$ and $\mu_i^v = 60\%$ for arteries, capillaries, and veins, respectively, according to ICRP report 89 (figure 5). The probability of a BP outflowing from compartment i to j is zero if the BP is in the artery or capillary sub-compartments $p_{i \rightarrow j}^a + p_{i \rightarrow j}^c = 0$. Only the vein reservoir has a non-zero probability of flowing out of the overarching compartment $p_{i \rightarrow j}^v = p_{i \rightarrow j}$ (equation (4)). The attenuation time of a single BP can be expressed as:

Figure 5. Relative blood volume capacity of the different vessel forms: arteries (red), capillaries (pink), and veins (blue).

$$\tau_i \in [\mu_i^a + \mu_i^c; 1] * \overline{\tau_i} \vdash \dashv \overline{\tau_i} \approx \frac{b_V^i * V_B}{CO * b_F^i}, \tag{5}$$

where $\overline{\tau_i}$ is the mean transition time of compartment i. The shortest attenuation time equals the propagation time through arteries and capillaries, which can be freely set by the user.

2.2.3. Customized hemodynamics

We proposed a method that enables us to tailor standardized flow rates and organ blood volumes references, such as those proposed by ICRP89, for individual patient's simulation through considering additional information about their individual blood flow. Due to the unavailability of a patient's hemodynamics data in this work, we optimized the regional blood volume of the BFM to achieve a dilution curve that closely resembles a published realistic dilution curve resulting from full-body circulation. This data comprises measured P^{32} labeled erythrocytes in the blood circulation at different timepoints after intravascular injection in a healthy subject (Nylin and Celander 1950). To reduce the complexity of the non-deterministic flow routes of BPs, we considered some simplifications about the heuristic flow behavior of BPs:

1) After traversing its route, a BP comes always back to its starting position O, which is assumed to be the vein compartment.

2) In each re-circulation, a BP must flow through the pulmonary circuit (i.e. heart, lung, aorta). A queue of traversed compartments $\mathscr{C}_k = \{O, \mathscr{C}_i, ..., \mathscr{C}_n\}$ after a time t is: $O_1 \rightarrow \mathscr{C}_{i^1} \rightarrow \mathscr{C}_{j^1} \rightarrow \mathscr{C}_{k^1} \rightarrow O_2 \rightarrow \mathscr{C}_{i^2} \rightarrow \mathscr{C}_{j^2} ... \rightarrow O_{x(t)}$. i^1 is the organ traversed at cycle 1 and $i^1 \neq i^2$ are two organs differing from each other. $O_{x(t)}$ is the most likely xth cycle that can be reached after a time t.

3) The BPs are not well mixed. The number of possible routes is finite. Each route is considered as a sequence of individual sub-paths which are traversed with an unknown flow rate to reach certain compartment at the time point of the measurement (t). For a particular path:

$$\rho_k(t) = \rho_0 \sum_{m=1}^{M} \prod_{k=1}^{n(t)} p_{T,k}^m(\rho_k), \tag{6}$$

where ρ_0 is the initial distribution of labeled BPs that are injected into the vein compartment. $\rho_k(t)$ is the number of labeled BPs reaching the compartment k at the time t. $p_{T,k}^m$ is the probability of particle m to be transferred from $k \rightarrow k+1$ compartment at the time T. If the time point of measurement t is shorter than accumulated transition times over the path queue $t < \sum_k^T \frac{V_k}{F_k}$ then $p_{T,k}^m(\rho_k) = 0$ and if a particle reaches the final compartment (i.e. vein) within a margin of $\delta = 1$ second $|t - \sum_i^n \overline{\tau_i}| \leqslant \delta/2$, the transition probability can be described by a series of blood volumes (V_k) and flow rates (F_k), $p_{T,k}^m(\rho_k) \approx \Sigma^m \sum_k^T \frac{V_k}{F_k}$. The product in equation (6) describes the blood fraction arriving from $1 \rightarrow n$ compartment at each consecutive time point (t) and the sum is the accumulation of arriving BPs over the permutation of flow paths. Optimal flow rates can be computed by minimizing difference between accumulated labeled BPs in the vein at each consecutive time point

Table 1. Input parameters for the optimization.

Parameter	Details	Value applied
α	Cooling rate	0.92
T_0	Initial temperature	250
maxIteration	Maximum number of iterations	3000
TolFunc	Stopping criteria: change value of the objective function	1e-4

$\rho^*(t)$ with respect to the measurement values ρ_{ref}:

$$\min_{p_T(\rho_k)\in P_T^*} \left(\frac{\rho_k^*(t)}{\rho_0} - \rho_{\mathrm{ref}}(t) \right)$$
$$0 < p_T^l \leqslant p_T \leqslant p_T^u. \tag{7}$$

p_T^l and p_T^u are lower and upper bounds of the interval of acceptable parameter values of V_k and F_k. To a first approximation, we set the interval to be restricted to an offset of $\pm 20\%$ around hemodynamics references and the positivity constraint to ensure that blood doesn't flow backward.

In this work, our focus was solely on optimizing the regional blood volume. The optimization was performed using the Simulated Annealing optimization technique, which easy to implement and is well-suited for solving large combinatorial optimization problems and thus aligned with our requirements (Kirkpatrick 1983, Aarts and Korst 1989). We applied the common exponential annealing schedule (Kirkpatrick 1983). Both the cooling rate α and the initial temperature T_0 were pre-selected empirically to ensure satisfactory convergence and runtime performance. Details of the input parameters used in optimization scheme can be found table 1.

2.3. The effect of protracted fraction delivery period

2.3.1. Treatment fraction delivery time and patient selection
To investigate how such delivery time prolongation affects the dose to CB, we developed a dynamic delivery method to simulate different scenarios of IMRT plans. A planning computed tomography (CT) and the corresponding delineated RT structures used in this work are publicly available at the Cancer Imaging Archive data repository (Clark *et al* 2013). The CT data is a part of the Glioma Image Segmentation for Radiotherapy study (Shusharina and Bortfeld 2021). The CTV volume is 236.3 cm^3. A fractionated clinical IMRT plan of 30×2 Gy fraction^{-1} was calculated using version 13.7 of the Eclipse treatment planning system (Varian Medical Systems, Palo Alto, California, USA). The plan consists of 6 fields (see figure 7).

2.3.2. Impact of the number of the segments
We assume that each fraction delivery is composed of N fields and n segments per field. For the sake of simplicity, the pulse widths of the ith field Δt_i are equally spaced in time and can be calculated:

$$\overline{\Delta t} = \frac{D_p}{N * n * \overline{\dot{D}}}, \tag{8}$$

where D_p is the total dose and the mean dose rate $\overline{\dot{D}} = 3$ Gy min^{-1}. The average time to change the MLC shape from the previous opening is $\overline{\varepsilon} = 7$ s (Wang *et al* 2003). The treatment delivery time of a single fraction can be described as:

$$T_F = n * \sum_i^N \overline{\Delta t} + (n - N + 1) * \overline{\varepsilon} + (N - 1) * \Delta t_G, \tag{9}$$

where $\Delta t_G \in [30, 60]$ second is the time necessary to reorientate the gantry and couch. The treatment time rises linearly with the number of segments n. We simulated different treatment times $T_F = \{7, 9, 13, 18\}$ min, assuming different segment counts per field $n = \{3, 5, 12, 20\}$, respectively (figures 6(a&b)).

2.3.3. Impact of non-uniform instantaneous dose rate of a realistic IMRT plan
The instantaneous dose rate varies continuously, and the number of segments is typically not constant and depends on the complexity level of the plan, resulting in a highly varying spatiotemporal dose distribution through the treated organ. We have (in analogy to section 2.3.2) simulated a realistic IMRT treatment delivery assuming varying $\dot{D}(t)$ and pulse width. Wang *et al* (2003) proposed that segment number, MLC motion time and pulse width can each be approximated to follow a Gaussian distribution. A random segment number n^* is
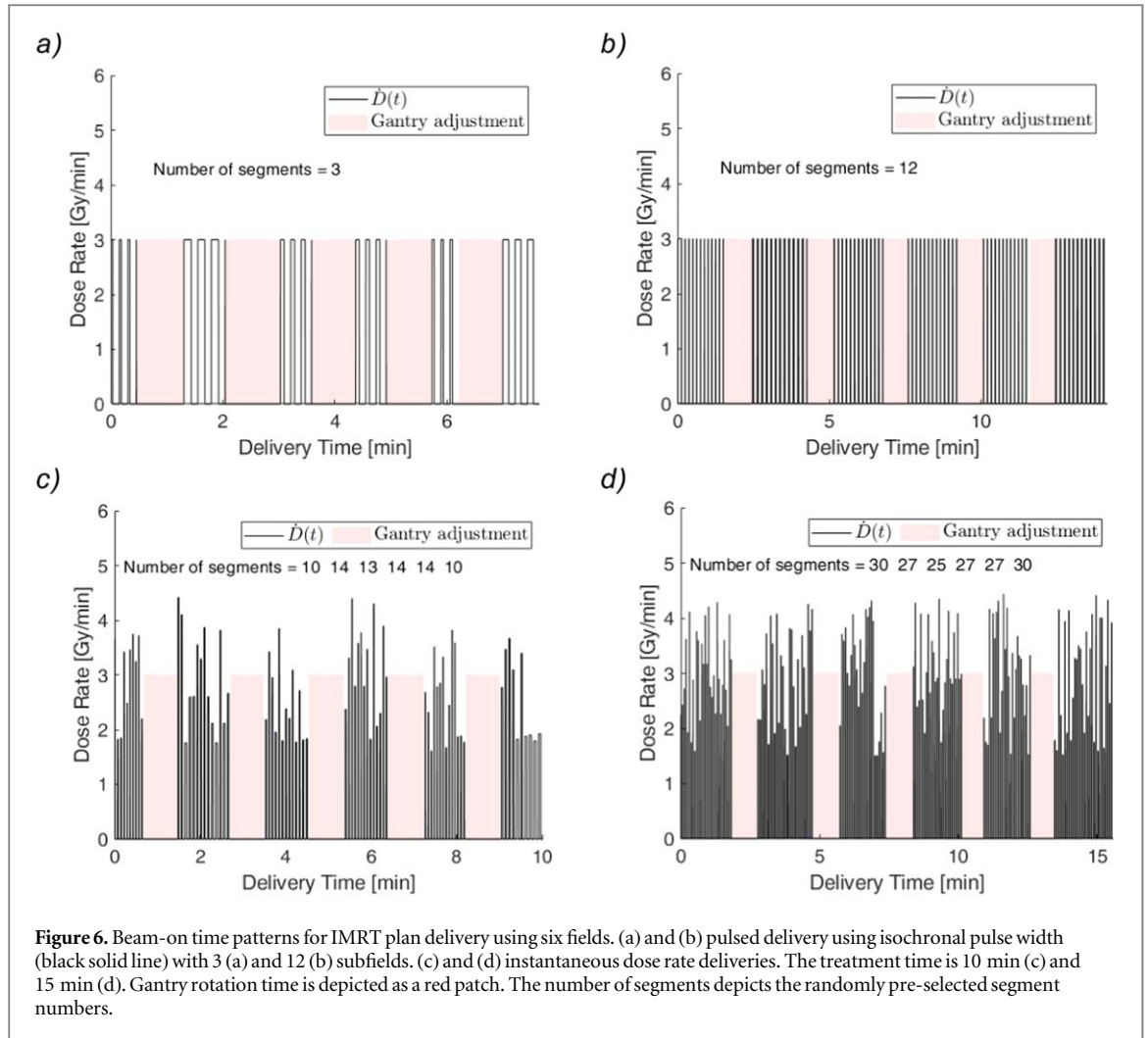
Figure 6. Beam-on time patterns for IMRT plan delivery using six fields. (a) and (b) pulsed delivery using isochronal pulse width (black solid line) with 3 (a) and 12 (b) subfields. (c) and (d) instantaneous dose rate deliveries. The treatment time is 10 min (c) and 15 min (d). Gantry rotation time is depicted as a red patch. The number of segments depicts the randomly pre-selected segment numbers.

drawn from interval $[n^l, \ n^u]$, where n^l, n^u are lower and upper segment counts, respectively. $\dot{D}_k$ varies with segment number, where $k = \{1, \ 2, \ ..., n^*\}$ and is uniform distributed $\dot{D}_k \in \overline{D} \ast [1 - w^l, \ 1 + w^u]$, with w^l, w^u being boundary weights that can be freely set by the user. In this work $\dot{D}_k(t) \in [1.5, 4.5] \ \mathrm{Gy} \ \mathrm{min}^{-1}$. Pulse width $\Delta t_{\dot{D}_k}$ can be calculated by minimizing the difference between planned dose D_{pi} per field i and the integrated $\dot{D}_k$ over time:

$$\min_{\Delta t} = \sum_i^N \left(D_{p_i} - \sum_k^{n_i^*} \dot{D}_k . \tau_{\dot{D}_k} \right)^2, \tag{10}$$

where $\Delta t \sim \mathcal{N}(\overline{\Delta t}, \ \sigma_{\Delta t}^2)$ and $\sigma_{\Delta t}^2 = \overline{\Delta t}/4$ is the variance. The aperture shaping time can be sampled from the normal distribution $\varepsilon \sim \mathcal{N}(\bar{\varepsilon}, \ \sigma_\varepsilon^2)$, with mean $\bar{\varepsilon} = (T_F - N \ast n \ast \overline{\Delta t})/(n - N)$ and variance $\sigma_\varepsilon^2 = \bar{\varepsilon}/4$. T_F is the entire treatment time. We simulated four different scenarios with different numbers of segments and fraction times (see figure 6).

2.4. Simulation

We extended the cortical vascular model from 2.1 with a network of generic vessels, assuming an isotropic distribution of the blood supply (similar to the approach proposed by Hammi *et al* (2020)) to guarantee blood supply to the entire brain volume. The entire vascular cerebral model was co-registered to the planning CT coordinates system (see figure 8d). The blood pool contains 42.125×10^6 BPs. The volume of a single BP is 1.25 μl. The brain contains 1.2% of the blood, corresponding to 5.3×10^5 BP. The time resolution of the d-BFM is $T_{\mathrm{BFM}} = 10^{-3}$ s. Each BP has seven parameters: ID number, intrinsic coordinates according to the RT-plan, speed, the compartment where it is located, the attenuation time in the current compartment τ_i, the accumulated dose D_i, and the number of irradiation hits. During beam-on, the instantaneous dose to the ith BP is computed by integrating its travel time t through the spatiotemporal local dose rate:
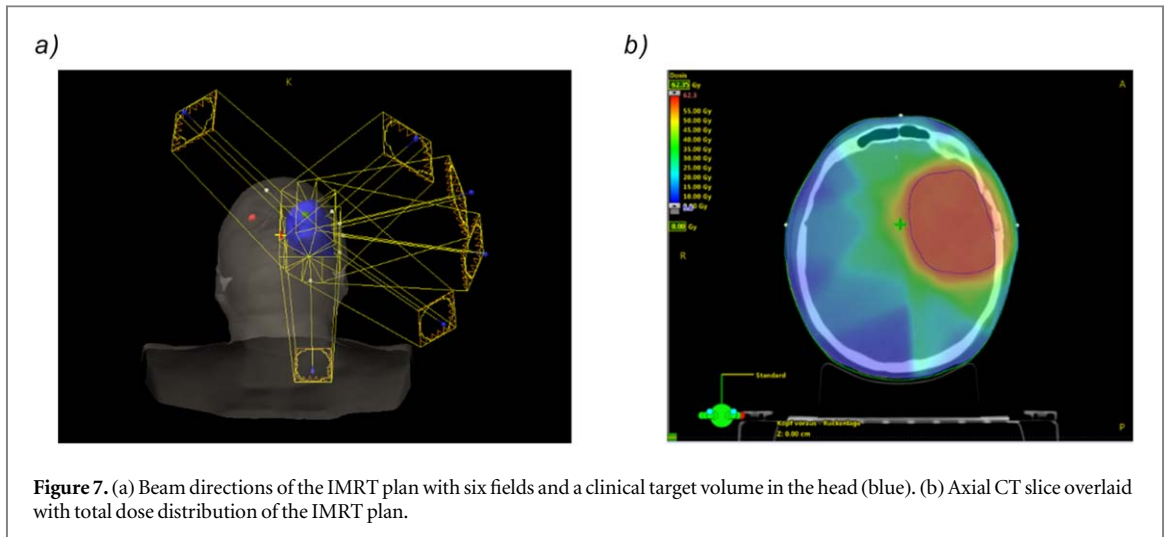
Figure 7. (a) Beam directions of the IMRT plan with six fields and a clinical target volume in the head (blue). (b) Axial CT slice overlaid with total dose distribution of the IMRT plan.

$$D_i = \dot{D} *_* \Delta t, \tag{11}$$

where $p(x, t, i)$ is the time-dependent path line of the ith BP, T_{BFM} is the time resolution of the d-BFM and $V(x)$ is the blood speed at that path.

During the gantry and couch adjustment time Δt_G, the beam is turned off. Since this period varies depending on the arc length that the gantry needs to travel between consecutive fields, we implemented a queuing approach that records the IDs and last location of each single BP of the blood pool just after turning off the beam and by using the formalism described in section 2.2.3, the future BPs distribution after time Δt_G can be computed to enable the d-BFM to localize single BPs at the time point when the next beam of the delivery is turned on.

We simulated one fraction for each of the scenarios (see sections 2.3.2 and 2.3.3 and table 2). The prescribed dose was 2 Gy. We calculated the DVHs of the CB in each scenario and we evaluated different dosimetric references, such as the minimum dose to the top 2% of blood volume $D_{2\%}$, $V_{D>0\text{Gy}}$ and $V_{D=0.07\text{Gy}}$ (this dose threshold corresponds to a lethal dose that reduces lymphocytes population from 100% to 98% (Nakamura *et al* 1990).

3. Results

3.1. Vasculature explicit blood flow

Figure 8 depicts different stages of the development of the cerebral vasculature model based on the formalism in chapter 2.1. The vasculature follows the topographic cortical surface. Figure 8(a) shows the true extracted macroscopic vessels, such as Circle of Willis, middle cerebral arteries, carotids arteries and superior longitudinal sinus. Figure 8(b) shows a fraction of the reconstructed surficial arteries. Figure 8(c&d) depict two different perspectives of the surficial vessels after applying the multiple topographic blood path lines approach. Figure 8(e&f) show the cerebral vasculature model co-registered to the patient planning CT. The phantom counts more than 850 vasculature path lines in total, 561 of which are patient-specific and 293 are generic straight path lines.

3.2. Optimized hemodynamic values

Figure 9 shows the transition diagram of the human d-BFM. Both a systemic and a pulmonary circuit model are considered. In this compact exemplification, we abstracted the considered organs into three nested compartments each: artery, capillary, and vein (bold lines), to improve the illustration. Table 3 presents a detailed list of the regional blood volume obtained from customizing the hemodynamics. The Simulated Annealing tests were performed on a 64 bit 16 GB CPU architecture. The optimization process succeeded in significantly decreasing the root-mean-square error among the dilution curves, with a variable runtime spanning (1 min—2.9 h). The computation runtime was dependent on the total number of BPs in the system, the cooling rate, and the duration of the measured dilution curve. Table 3 illustrates the outcome of customizing the hemodynamics before and after the optimization process.

Figure 10 shows a comparison between the measured dilution curve of a healthy subject and the resulting dilution curve of the d-BFM before and after optimizing the adjacent matrix. The concentration flow values (y-axis) were normalized. The delay time between the injection time point and the time of the first concentration detection ($t = 9$ s) and the rapid concentration increasing matches very well with the measurements. The width
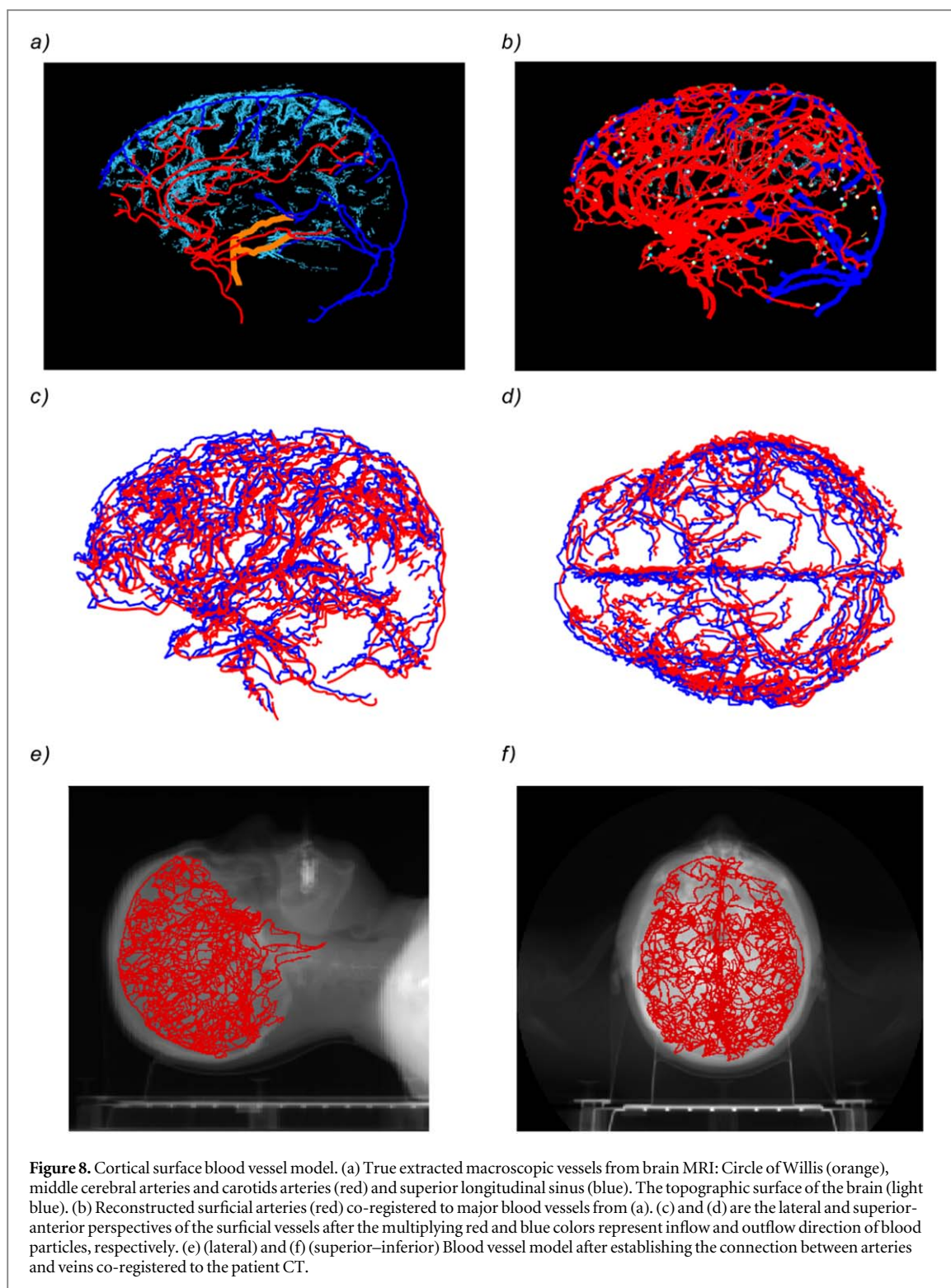
Figure 8. Cortical surface blood vessel model. (a) True extracted macroscopic vessels from brain MRI: Circle of Willis (orange), middle cerebral arteries and carotids arteries (red) and superior longitudinal sinus (blue). The topographic surface of the brain (light blue). (b) Reconstructed surficial arteries (red) co-registered to major blood vessels from (a). (c) and (d) are the lateral and superior-anterior perspectives of the surficial vessels after the multiplying red and blue colors represent inflow and outflow direction of blood particles, respectively. (e) (lateral) and (f) (superior–inferior) Blood vessel model after establishing the connection between arteries and veins co-registered to the patient CT.

Table 2. Simulated treatment delivery scenarios of the IMRT plan.

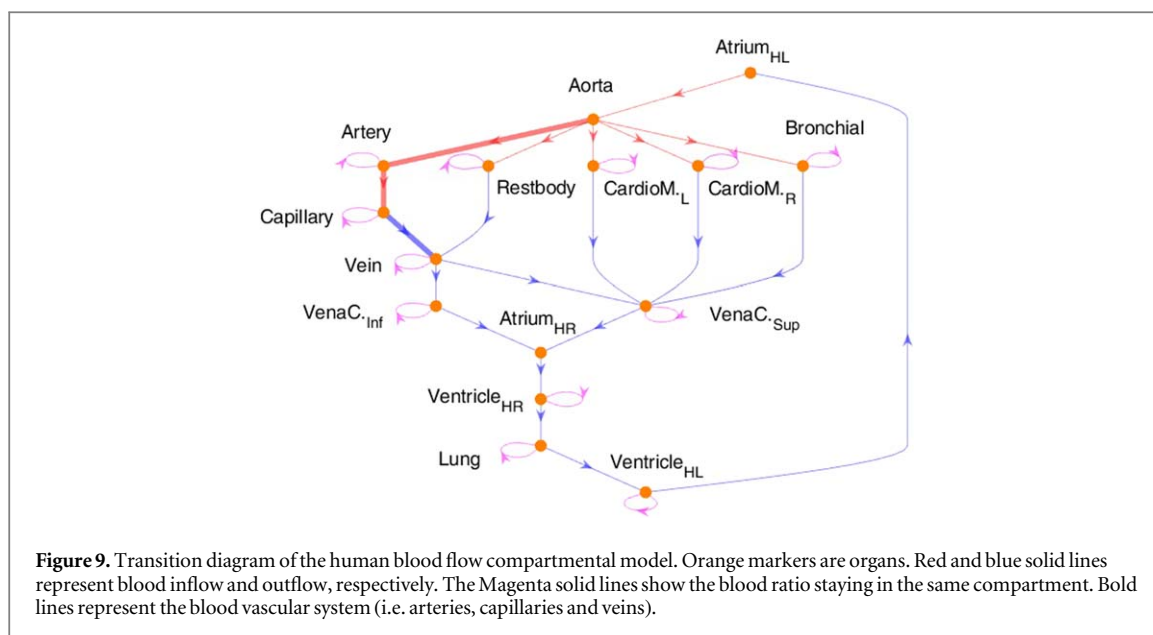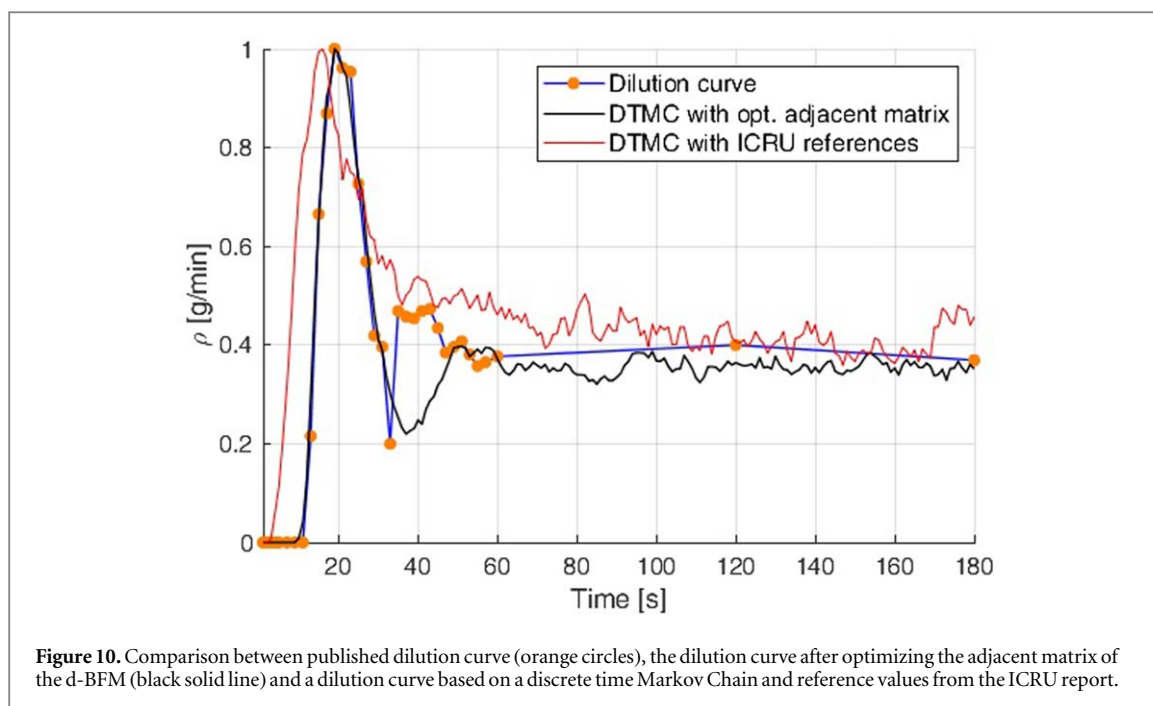| Configuration	Segment numbers	Fraction time
scenario 1	[10, 15]	10 min
scenario 2	[20, 25]	10 min
scenario 3	[20, 25]	15 min
scenario 4	[25, 30]	15 min

Figure 9. Transition diagram of the human blood flow compartmental model. Orange markers are organs. Red and blue solid lines represent blood inflow and outflow, respectively. The Magenta solid lines show the blood ratio staying in the same compartment. Bold lines represent the blood vascular system (i.e. arteries, capillaries and veins).

Table 3. Comparison between relative reference values for organ blood volumes and blood flow rates in adults from ICRP report 89 and after optimization.

Organ	ICRP references		Optimized values	
	Blood volume [%]	Flow rate [%]	Blood volume [%]	Flow rate [%]
Brain	1.2	12	1.2	12
Right heart	4.5	—	4.3	—
Left heart	4.5	—	4.2	—
Coronary tissue	1	4	1.2	4
Pulmonary	10.5	—	9.8	—
Bronchial tissue	2.0	2.5	1.9	2.5
Fat	5.0	5.0	4.7	5.0
Stomach	1.0	1.0	0.9	1.0
Small intestine	3.8	10	4.5	10
Large intestine	2.2	4.0	2.7	4.0
Kidneys	2.0	19	2	19
Liver	10.0	25.5	12	25.5
Skeletal muscle	14.0	17	13.6	17
Pancreas	0.6	1.0	0.6	1.0
Skeleton and bone	7.0	5.0	8.5	5.0
Skin	3.0	5.0	3.3	5.0
Spleen	1.4	3.0	1.3	3.0
Thyroid	0.06	1.5	0.06	1.5
Lymph nodes	0.2	1.7	0.2	1.7
Gonads	0.04	0.05	0.04	0.05
Adrenals	0.06	0.3	0.06	0.3
Bladder	0.02	0.06	0.02	0.06
other tissues	1.92	1.39	0.22	1.39
Large arteries	6	—	5.6	—
Large veins	18	—	17.1	—

of the first peak, the decay of the concentration gradient ($t > 20$ s) and the steady state distribution ($t > 60$ s) all agree well with measured concentrations. However, the derived peak of the second circulation ($t = 42$ s) escalates slower than the measured data. The comparison with a dilution curve calculated using DTMC and without optimization of the ICRU report 89 reference values shows that the delay period is shorter (3 s). This is, however,

Figure 10. Comparison between published dilution curve (orange circles), the dilution curve after optimizing the adjacent matrix of the d-BFM (black solid line) and a dilution curve based on a discrete time Markov Chain and reference values from the ICRU report.

unavoidable because the simplified model using DTMC does not consider the constrained queuing of the BPs (i.e. arteries and capillary) and the resulting attenuation time.

3.3. The effect of protracted fraction delivery on dose to circulating blood

3.3.1. Impact of prolonged delivery time
The resulting DVHs of CB as a function of the segments counts and the treatment time are shown in figure 11. The treatment time ranges from 7 to 18 min. It becomes clear that increasing segment numbers augments the CB fraction getting any dose $V_{D>0Gy}$ while it reduces the volume fraction receiving a high dose. $D_{1\%}$ was found to be the highest during the delivery with the smallest segment number (i.e. 3 segments) and decreased with increasing the delivery time. The CB volume receiving at least $D= 0.07$ Gy is twice as high as in the case of 5 segments and over 22 times higher than in the case of 12 segments. The results are summarized in table 4. This analysis highlights the trade-off between CB volume fractions receiving low and high doses. Figures 12(a&b) show the evolution of the accumulated blood volume receiving any dose $D > 0$ Gy and $D = 0.07$ Gy during a single fraction as a function of the number of the delivered fields.

3.3.2. Impact of the non-uniform instantaneous dose rate of a realistic IMRT plan
Figure 13(a) depicts DVHs for different realistic delivery scenarios calculated using the approach described in 2.3.3. The total segment counts are 75, 139, 132 and 166 for scenario 1, 2, 3 and 4, respectively. The DVHs are characterized by extended high-dose tails. In both cases, increasing segment numbers without changing the fraction delivery time, or increasing treatment time without changing segment numbers, resulted in augmenting of low-dose regions and a reduction of the blood volume fraction receiving a high dose. The disparity of the dose distribution is, however, less significant when the treatment time is kept identical. In all scenarios, the threshold $D= 0.07$ Gy was not reached. The blood fraction receiving any dose $V_{D>0Gy}$ are shown in figure 13b. This volume fraction is less affected by the segment counts when the treatment time is identical, but more dependent on the treatment time. Table 5 contains a summary of the dosimetric values of the scenarios.

4. Discussion

The purpose of this study was to develop a dosimetric pipeline that enables investigating the accumulated radiation dose absorbed by the peripheral blood pool during external radiation treatment for tumor patients.

The in-house developed image-based model to extract cortical vessels was found to reconstruct the real-world configuration of the cerebrovasculature. We believe that automating blood vessel extraction can improve the quality and reproducibility of blood flow models, as well as yielding considerable time savings through avoiding manual delineation. In addition, it can be applied to standard MRI data of the patient, which opens the door to customizing the vasculature architecture to the personalized anatomy of the patient's brain to improve
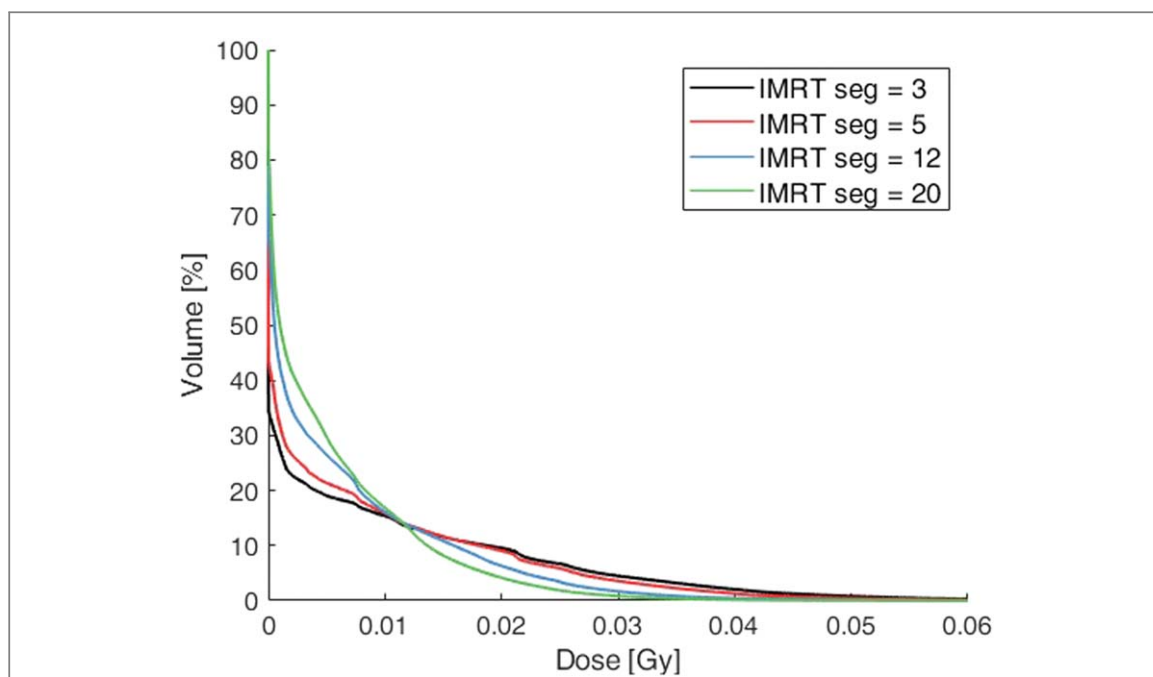
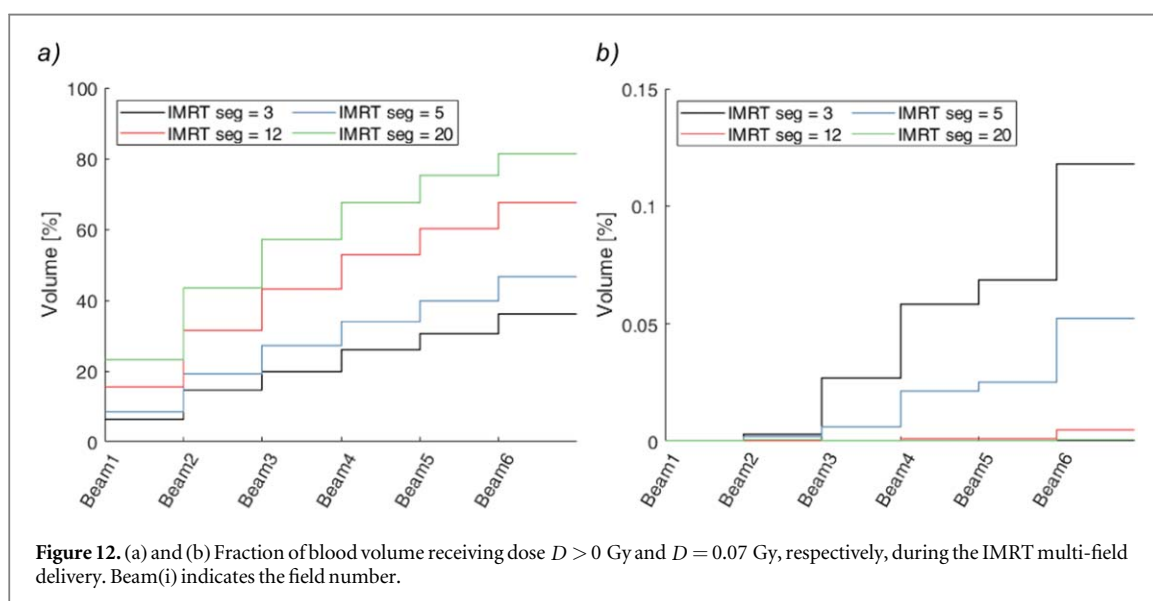**Figure 11.** DVHs for different fraction deliveries with different segment numbers.

Figure 12. (a) and (b) Fraction of blood volume receiving dose $D > 0$ Gy and $D = 0.07$ Gy, respectively, during the IMRT multi-field delivery. Beam(i) indicates the field number.

Table 4. Summary of dosimetric parameters.

Segments number/field	Seg 3	Seg 5	Seg 12	Seg 20
$V_{D>=0\ \text{Gy}}$ [%]	36.16	46.43	67.39	81.49
$V_{D=0.07\ \text{Gy}}$ [%]	0.120	0.052	0.005	0.001
$D_{V=2\%}$ [Gy]	0.090	0.080	0.061	0.005

the accuracy of the blood flow modeling inside the treated organs. The cortical topographic vessel technique still requires further improvements to detect even more deeply located blood vessels to guarantee homogeneous blood supply inside the brain while reducing the application of generic blood path lines. However, this model constitutes an increase of over 1300% compared to the previous models that contained only 5% of realistic vasculature (see Hammi *et al* 2020).
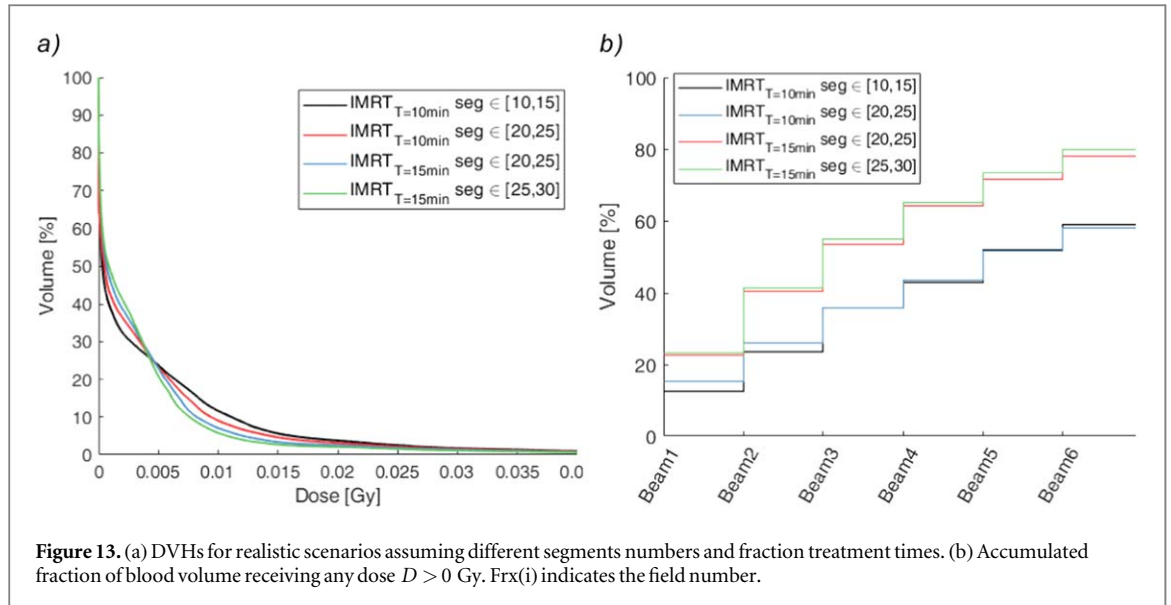
Figure 13. (a) DVHs for realistic scenarios assuming different segments numbers and fraction treatment times. (b) Accumulated fraction of blood volume receiving any dose $D > 0$ Gy. Frx(i) indicates the field number.

Table 5. Summary of dosimetric parameters of the instantaneous dose rate delivery.

Scenario	1	3	3	4
$V_{D>=0\text{Gy}}$ [%]	59.03	57.84	77.96	79.72
$V_{D=0.07\text{Gy}}$ [%]	0.06	0.05	0.043	0.036
$D_{V=2\%}$ [Gy]	0.084	0.082	0.08	0.078

Algorithm 1. Description of the approach to search for multiple trajectories of different topography around the shortest trajectory that connects source-target nodes.

Input: Graph: Set of nodes $v^{\,i} = \{v^1, \ldots, v^n\}$, source node: S, destination nodes: T, must-connect nodes c, radii r
Output: paths from source to destination nodes: P
Define a graph $G(v,\ e,\ w)$ with positive weights $w: e \rightarrow \mathbb{R}^+$ for interconnecting edges e;
Initialize starting and corresponding destination nodes $s = \{s^1, \ldots, s^m\}$; $t = \{t^1, \ldots, t^m\}$;
$\leftarrow \varnothing$ a set of path lines
For $i(1 \leqslant i \ldots m)$**do**
Preselect a set of sequential control nodes $c_i^k = \{c_i^1, \ldots, c_i^q\} \in P^i$;
predefined threshold radii $r_i^k = \{r_i^1, \ldots, r_i^q\}$;
For $j(1 \leqslant j \leqslant q - 1)$ **do**
Use Dijkstra's approach to compute the shortest distance L_j between sequential control nodes pairs $w_{\text{path}}(c_i^j, c_i^{j+1}) = \sum_k \min_{v_k \in L} t(v_k)$

$P^i \leftarrow P^i \cup \{L_j\}$
For all $v_k \in L_j \subseteq v$ do
For $u \in v$ do
Pick up new node-set candidates u
If $w(v_k,\ u) \leqslant r_i^j$
$P^i \leftarrow P^i \cup \{u\}$
End
End
End
End
return P^i

From the analysis of the shape of the dilution curves derived from the optimized hemodynamics model compared to those obtained from a non-optimized model that relies solely on ICRP89 references and DTMC, it becomes evident that the optimized hemodynamics model generates a more similar blood mixing across the entire body to published data, as the latter model.

This agreement gives us confidence that optimizing the hemodynamics of the BFM results in a more realistic simulation of the blood mixing process. We believe it is crucial to account for both blood flow rate and blood volume of the individual patient's organs and to consider intra- and inter-subject hemodynamics variation to achieve precise estimation of the absorbed dose to the circulating lymphocytes, especially inside organs with higher flow rate to blood volume ratio (e.g. brain, kidney, liver…). The dilution curve used in our study to benchmark our d-BFM was not specifically obtained for the purpose of this study. It originates, however, from other measurements of a healthy subject, and some useful information about the conditions of the experiments, such as the injected amount of the labeled blood, is not provided. Therefore, more subject regional blood flow measurements are still needed to evaluate the reliability of the approach when considering large subject inter-variation. The approach in 2.2.3 can be further improved by considering the transmission time of BP inside the compartment to improve the optimization step.

The evaluation of the dosimetric difference between step-and-shoot and dynamic delivery showed that constant dose rate delivery substantially affects the dose distribution received by peripheral blood compared to deliveries based on instantaneous dose rates. This is solely because of the additional prolonged time of a single fraction. The results show that non-uniform instantaneous delivery impacts the dose distribution of the CB only slightly when prolonged time is kept unchanged and just long enough to deliver the total prescribed dose fraction. As a rule of thumb, when the beam-off time is non-uniform distributed negates the effect of prolonged time resulting from the count of the segments applied. Such a fact opens the question of how more modern techniques (e.g. sliding window IMRT, VMAT) affect the dose received by CB, since both techniques slide the aperture continuously. Therefore, the dynamic delivery designed for this study needs to be extended to enable simulating such state-of-the-art techniques. In addition, in this work, we considered only photons, but other treatment modalities, such as proton pencil-beam scanning, are subject of future planned studies.

There were several limitations of this study. To a first approximation, we assumed that the total dose delivered from a single field is the aggregation of all the individual dose contributions from the segments representing this field. Although we considered continuously varying dose rates of individual segments, we simplified our delivery model by assuming the spatial dose distribution to be identical. In addition, the scattering terms arising from the collimation were not considered.

The estimated total lymphocyte population that circulates through the blood is estimated at 2%–5%, while the rest of the population is located inside the lymphoid organs (Blum and Pabst (2007). Our d-BFM does not consider the complex migration behavior of the lymphocytes between blood and lymphoid organs. Since the brain does not contain any lymphatic tissue, the dose to the circulating blood in the brain is then assumed to be the dose to the circulating lymphocytes.

The results of the framework presented in this study are limited by the abstractions applied to the designed dynamic delivery mode and by the approximations used to compensate for lack of reliable information about human hemodynamics. Nevertheless, all parameters used to develop this model stem from peer-reviewed publications and are therefore assumed to be state-of-the art.

5. Conclusion

In this work, we have developed a dosimetric whole-body blood flow model that enables us to explicitly track blood particles in the brain and calculate the accumulated dose to the circulating blood during external radiation therapy. We presented an approach to individualize the hemodynamic parameters of the d-BFM to individual patients by considering patient-specific information. Prolonged treatment delivery of IMRT affects the accumulated dose distribution received by the CB during fractionated radiation therapy. Investigating different delivery parameters and how they affect the dose to the circulating lymphocytes will allow us to better understand radiation-induced lymphopenia and could open the door to optimizing and tailoring the delivery to reduce lymphocyte depletion.

Acknowledgments

Data availability statement

The data cannot be made publicly available upon publication because they are owned by a third party and the terms of use prevent public distribution. The data that support the findings of this study are available upon reasonable request from the authors.

ORCID iDs

Abdelkhalek Hammi ⓘ https://orcid.org/0000-0002-4001-1180

References

Aarts E H and Korst J 1989 *Simulated Annealing and Boltzmann Machines: A Stochastic Approach to Combinatorial Optimization and Neural Computing* (Chichester: Wiley)

Absinta M *et al* 2017 Human and nonhuman primate meninges harbor lymphatic vessels that can be visualized noninvasively by MRI *Elife* **6** e29738

Aymeric L *et al* 2010 Tumor cell death and ATP release prime dendritic cells and efficient anticancer immunity *Cancer Res.* **70** 855–8

Basler L *et al* 2018 Modelling the immunosuppressive effect of liver SBRT by simulating the dose to circulating lymphocytes: aninsilico planning study *Radiat. Oncol.* **13** 10

Blum K S and Pabst R 2007 Lymphocyte numbers and subsets in the human blood Do they mirror the situation in all organs? *Immunol. Lett.* **108** 45–51

Cho Y *et al* 2019 Impact of treatment-related lymphopenia on immunotherapy for advanced non-small cell lung cancer *Int. J. Radiat. Oncol. Biol. Phys.* **105** 1065–73

Clark K *et al* 2013 The cancer imaging archive (TCIA): maintaining and operating a public information repository *J. Digit. Imaging* **26** 1045–57

Contreras J A, Lin A J and Weiner A 2018 Cardiac dose is associated with immunosuppression and poor survival in locally advanced non-small cell lung cancer *Radiother. Oncol.* **128** 498–504

Correia M P *et al* 2016 4D ultrafast ultrasound flow imaging: *in vivo* quantification of arterial volumetric flow rate in a single heartbeat *Phys. Med. Biol.* **61** L48–61

Diehl A, Yarchoan M and Hopkins A 2017 Relationships between lymphocyte counts and treatment-related toxicities and clinical responses in patients with solid tumors treated with PD-1 checkpoint inhibitors *Oncotarget* **8** 114268–80

Dijkstra E W 1959 A note on two problems in connexion with graphs *Numer. Math.* **1** 269–71

Duvernoy H M 1999 *The Human Brain: Surface, Blood Supply, and Three-dimensional Sectional Anatomy* (Berlin: Springer)

Hammi A, Paganetti H and Grassberger C 2020 4D blood flow model for dose calculation to circulating blood and lymphocytes *Phys. Med. Biol.* **65** 055008

Ho W J, Yarchoan M and Hopkins A 2018 Association between pretreatment lymphocyte count and response to PD1 inhibitors in head and neck squamous cell carcinomas *Immunother. Cancer* **6** 84

Hoskins P R 1996 Accuracy of maximum velocity estimates made using Doppler ultrasound systems *Br. J. Radiol.* **69** 172–7

ICRP89 2002 Basic anatomical and physiological data for use in radiological protection reference values. A report of age- and gender-related differences in the anatomical and physiological characteristics of reference individuals *Ann. ICRP Publication 89* **32** 5–265

Jiang J *et al* 2011 Comparison of blood velocity measurements between ultrasound Doppler and accelerated phase-contrast MR angiography in small arteries with disturbed flow *Phys. Med. Biol.* **56** 1755–73

Joseph N, McWilliam A and Kennedy J 2019 Post-treatment lymphocytopaenia, integral body dose and overall survival in lung cancer patients treated with radical radiotherapy *Radiother. Oncol.* **135** 115–9

Kao C *et al* 2007 A geometric method for automatic extraction of sulcal fundi *IEEE Trans. Med. Imag.* **26** 530–40

Karantanos T, Karanika S and Seth B 2019 The absolute lymphocyte count can predict the overall survival of patients with non-small cell lung cancer on nivolumab: a clinical study *Clin. Transl. Oncol.* **21** 206–12

Kirkpatrick S, Gelatt C D and Vecchi M P 1983 Optimization by simulated annealing *Science Clin. Transl. Oncol.* **220** 671–80

Kleinberg L, Sloan L and Grossman S 2019 Radiotherapy, lymphopenia, and host immune capacity in glioblastoma: a potentially actionable toxicity associated with reduced efficacy of radiotherapy *Neurosurgery* **85** 441–53

Klug F *et al* 2013 Low-dose irradiation programs macrophage differentiation to an iNOS(+)/M1 phenotype that orchestrates effective T cell immunotherapy *Cancer Cell* **24** 589–602

Leggett R W and Williams L R 1995 A proposed blood circulation model for Reference Man *Health Phys.* **69** 187–201

llavena P *et al* 2008 The Yin-Yang of tumor-associated macrophages in neoplastic progression and immune surveillance *Immunol. Rev.* **222** 155–61

Nakamura N, Kusunoki Y and Akiyama M 1990 Radiosensitivity of CD4 or CD8 positive human T-lymphocytes by an *in vitro* colony formation *Radiat. Res.* **123** 224–7

NgA J M 2001 On spectral clustering: analysis and an algorithm *Advances in Neural Information Processing Systems* **14** 849–856

Ni J *et al* 2012 Sustained effector function of IL-12/15/18-preactivated NK cells against established tumors *J. Exp. Med.* **209** 2351–65

Nylin G and Celander H 1950 Determination of blood volume in the heart and lungs and the cardiac output through the injection of radiophosphorus *Circulation* **1** 76–83

Perona P and Malik J 1990 Scale-space and edge detection using anisotropic diffusion, pattern analysis and machine intelligence *IEEE Trans.* **12** 629–39

Shin J X *et al* 2021 HEDOS-a computational tool to assess radiation dose to circulating blood cells during external beam radiotherapy based on whole-body blood flow simulations *Phys. Med. Biol.* **66** 10

Shusharina N and Bortfeld T 2021 Glioma image segmentation for radiotherapy: RT targets, barriers to cancer spread, and organs at risk [Data set] *Cancer Imaging Archive* Retrieved from (https://doi.org/10.7937/TCIA.T905-ZQ20)

Wang J Z *et al* 2003 Impact of prolonged fraction delivery times on tumor control: a note of caution for intensity-modulated radiation therapy (IMRT) *Int. J. Radiat. Oncol. Biol. Phys.* **57** 543–52

Wu C Y *et al* 2014 Enhanced cancer radiotherapy through immunosuppressive stromal cell destruction in tumors *Clin. Cancer Res.* **20** 644–57

Xing S *et al* 2022 A dynamic blood flow model to compute absorbed dose to circulating blood and lymphocytes in liver external beam radiotherapy *Phys. Med. Biol.* **67** 10

Yovino S *et al* 2013 The etiology of treatmentrelated lymphopenia in patients with malignant gliomas: modeling radiation dose to circulating *Cancer Invest.* **31** 140–4

Zarrinkoob L *et al* 2015 Blood flow distribution in cerebral arteries *J. Cerebral Blood Flow Metab.* **35** 648–54

Zhuang B S *et al* 2021 The role of 4D flow MRI for clinical applications in cardiovascular disease: current status and future perspectives *Quant. Imaging Med. Surg.* **11** 4193–210